LASER & PHOTONICS REVIEWS
www.lpr-journal.org

High-Resolution 2D Quasi-Distributed Optical Sensing with On-Chip Multiplexed FSR-Free Nanobeam Cavity Array

Renjie Tang, Chunlei Sun, Kangjian Bao, Zequn Chen, Zezhao Ju, Maoliang Wei, Yingchun Wu, Jianghong Wu, Kai Xu, Hongtao Lin, and Lan Li**

On-chip free spectral range (FSR)-free optical filter with a compact footprint is crucial for developing emerging sensing applications, as it allows for the optimal utilization of extensive optical bandwidth. Despite being an important area of technology, on-chip optical sensing system has faced challenges in channel count, particularly due to the limited FSR, large footprint, and loss of the wavelength-selective filter unit. To address these challenges, a scalable nanobeam cavity prototype with a length of ≈21 µm based on the asymmetric Bragg mirrors is presented. By engineering the band structure of the nanobeam cavity, the stopband can be flexibly tuned to achieve an FSR-free spectral response within 350 nm. Two 25-nanobeam-cavity arrays are fabricated with a footprint of 215 × 120 µm^2 and an average insertion loss of ≈3.2 dB over a broad wavelength range. To the best of the authors' knowledge, this is the largest-channel-count multiplexed micro-cavity array on a single waveguide, reported to date. As a proof-of-principle application, the 2D high-spatial-resolution temperature distribution sensing is experimentally demonstrated. This work provides new insight into the design of ultra-compact FSR-free filters and will give birth to numerous charming applications that make use of the broad bandwidth capabilities of optics while occupying minimal space.

1. Introduction

The development of wavelength-selective optical filters has spurred growth in diverse information processing and optical sensing since this technology leverages multiple light wavelengths on a shared physical channel. To name a few, the integration of multiple wavelength-selective filters on a single optical link allows for the modulation or separate processing of different wavelength channels.[1–4] This type of multi-wavelength modulation can significantly improve the capacity, power and energy efficiency of optical communication or optical parallel computing, as the elimination of wavelength demultiplexing will be possible through the use of a microcomb source.[5–10] Furthermore, the optical filters may give birth to numerous new optical sensing applications with multiparameter advantages.[11] The sensing units working at different wavelengths are arranged according to specific rules, which can retrieve the spatial distribution information of various physical quantities such as temperature, concentration,[12] strain,[13] and even ultrasound[14,15] to achieve quasi-distributed sensing. Additionally, multiplexed functionalization with different bioreceptors allows for the simultaneous detection of multiple analytes from a single sample.[16]

Although arrayed waveguide grating (AWG) has achieved many physical channels,[17,18] it suffers from large device sizes and the inflexibility to independently control each channel. On the other hand, whispering gallery mode (WGM) cavities such as micro-ring/disk are compact and fundamentally provide resonant enhancement modulation/sensing, along with the inherent capability for wavelength multiplexing. Each WGM cavity in the array can be independently controlled with flexibility. However, due to the limited FSR, the number of channels in a WGM cavity array is difficult to increase (≤16).[2,15,19–21] By leveraging the vernier effect, it is possible to achieve a significantly larger FSR by cascading multiple micro-rings with varying FSRs.[22] However, the extended FSR is typically smaller than 100 nm due to the trade-off between the small radius and low bending losses. In addition, it is difficult to achieve the resonant wavelength alignment. An essential challenge is to develop a wavelength-selective filter with FSR-free and compact merits. FSR-free response with

R. Tang, C. Sun, K. Bao, Z. Chen, Y. Wu, J. Wu, L. Li
Key Laboratory of 3D Micro/Nano Fabrication and Characterization of Zhejiang Province
School of Engineering
Westlake University
Hangzhou 310030, China
E-mail: sunchunlei@westlake.edu.cn; lilan@westlake.edu.cn
R. Tang, C. Sun, K. Bao, Z. Chen, Y. Wu, J. Wu, L. Li
Institute of Advanced Technology
Westlake Institute for Advanced Study
Hangzhou 310024, China
Z. Ju, M. Wei, K. Xu, H. Lin
State Key Laboratory of Modern Optical Instrumentation
Key Laboratory of Micro-Nano Electronics and Smart System of Zhejiang Province
College of Information Science and Electronic Engineering
Zhejiang University
Hangzhou 310027, China

The ORCID identification number(s) for the author(s) of this article can be found under https://doi.org/10.1002/lpor.202300828

DOI: 10.1002/lpor.202300828

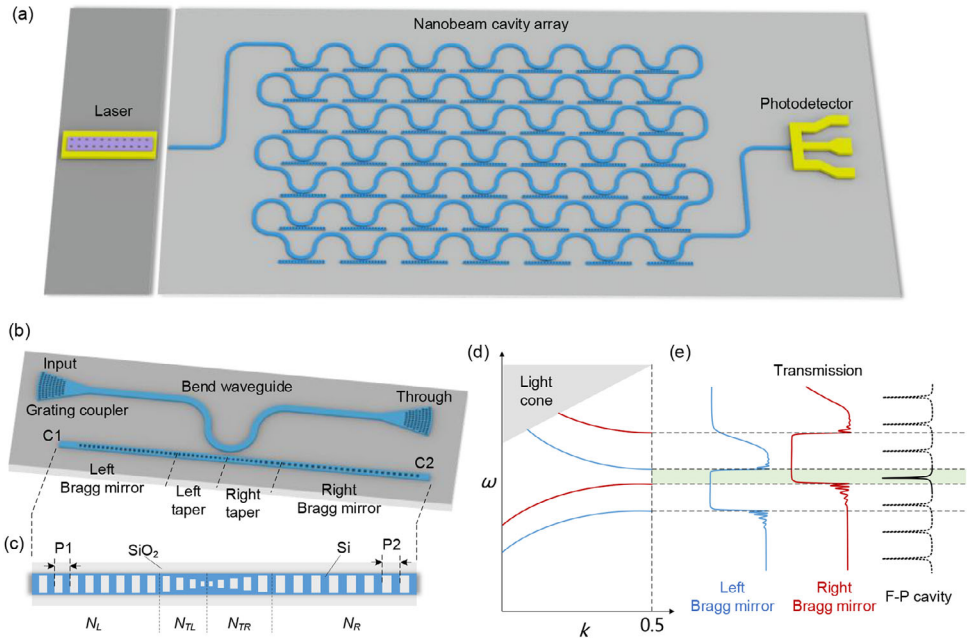

Figure 1. a) On-chip scalable wavelength-selective filter array. b) Schematic 3D view of SCAN cavity. c) Top view of the nanobeam cavity with asymmetric Bragg mirrors. d) Band structures of one unit cell for left (blue) and right (red) Bragg mirrors. e) Transmission spectra of the left (blue) and right (red) Bragg mirror and side-coupled F–P cavity (black).

narrow bandwidth is critical as it enables the cascading of numerous independent functional units on a single optical link, occupying little space and optimizing the wideband advantages of optics. Over the past decade, some FSR-free schemes have been proposed, such as Bragg grating waveguides/couplers[23–25] and Bragg-grating-assisted micro-ring.[26] Due to its photonic bandgap characteristics, a Bragg grating waveguide/coupler typically exhibits a response spectrum with a bandwidth ranging from a few nanometers to several tens of nanometers. While the use of weakly modulated gratings can reduce the bandgap width, this results in an excessively long grating length.[27–29] To achieve narrow bandwidth and FSR-free characteristics concurrently, one approach is to incorporate Bragg gratings into one or two coupling regions of the micro-ring. However, meeting the stringent requirements for design and fabrication tolerance is challenging. This approach ensures maximum side-mode suppression at undesired resonant wavelengths by attaining a stopband for the grating that is twice the micro-ring's FSR. Recently, we have demonstrated an FSR-free, wavelength-alignment-free and narrowband filter by side-coupled Bragg-grating-assisted (SCBGA) Fabry–Pérot (F–P) cavity.[30–32] This new approach compressed the stopband of the Bragg mirror to be smaller than the FSR of the F–P cavity, leading to an FSR-free response within 200 nm (limited to testing conditions). The length of the filter is typically >90 μm due to weak grating strength and using a large number of grating periods for high reflection.

On the other hand, a one-dimensional (1D) photonic crystal (PhC) nanobeam cavity can provide outstanding high-quality (Q) factor, small mode volume (V), and ultra-compact size properties, enabling numerous breakthroughs in quantum information processing,[33] optomechanics,[34,35] optical communication,[36] optical sensing[37–39] and many other areas.[40,41] These exciting applications in optical science benefit from the enhancement of light-matter interaction spatially (mode volume V) and temporally (Q-factor). In addition, owing to its simple geometry and ultra-compact size, the nanobeam cavity could have shown strong potential in arraying for large-scale multi-wavelength applications. Specifically, label-free quasi-distributed sensing at the single-cell scale (about tens of microns) may be realized through cascaded nanobeam cavities as the independent functional units on a single sensor link, as shown in **Figure 1**a. Although some individuals have claimed to have achieved FSR-free nanobeam cavities,[9] and certain experiments may appear to support this claim,[9,37] none of them have presented a response spectrum wide enough (≥100 nm) to provide conclusive evidence. In practice, the coexistence of multiple longitudinal modes in the cavity,[38,41–43] leads to the limited FSR. At present, the channel count of the nanobeam cavity array is small (≤5).[39,44–46]

In this work, we report a scalable nanobeam cavity prototype that overcomes the limitation of FSR by engineering the band structure of the nanobeam cavity in a novel way that excites only the fundamental longitudinal mode and suppresses the high-order modes in the cavity. This allows for FSR-free response while maintaining the small mode volume advantages of the nanobeam cavity. Unlike our previously reported SCBGA F-P cavity using symmetric Bragg mirrors,[30,31] which is difficult to be employed in the nanobeam cavity since the stopband of the Bragg mirror of the nanobeam cavity is quite large. While incorporating subwavelength holes in Bragg mirrors can effectively reduce the stopband, this approach comes at the cost of significantly increasing the device size and introducing considerable challenges in the fabrication process. Here, we employ asymmetric Bragg mirrors. Thus, the effective stopband, that is, the overlapping region of the stopband of the Bragg mirror on both sides, can be

flexibly engineered to be much narrower than the stopband of either of the individual stopbands. Only a deep dip within a large waveband of 350 nm is observed. Twenty-five basic units are cascaded in series, forming a 5 × 5 compact sensing matrix. Quasi-distributed temperature sensing with high position resolution is successfully achieved as a demonstration.

2. Results and Discussion

2.1. Device Design and Operation Principle

The schematic of a side-coupled asymmetric-nanobeam (SCAN) cavity is depicted in Figure 1b. It consists of a bent waveguide that feeds the light into the cavity. The typical design of a nanobeam incorporates a defect into the uniform pitch of the Bragg grating, resulting in the formation of an F–P cavity bounded by two Bragg mirrors. The compact footprint of the nanobeam cavity leverages the strong coupling strength of the Bragg mirrors, as per the coupled mode theory, to attain a high rejection ratio. As expected, the stopband of the Bragg mirror will be as large as several hundreds of nanometers for a silicon nanobeam cavity with a wavelength-scale mode volume. As reported in ref. [30], the key to attaining FSR-free response is to make the stopband smaller than the FSR of the F–P cavity. However, the stopband of the Bragg mirror of the nanobeam cavity is much larger than the FSR of the F–P cavity due to its strong mirror strength. Although incorporating small holes to increase the waveguide dielectric filling fraction can decrease the mirror strength, the cavity length and device footprint will increase simultaneously as a result. Meanwhile, the holes cannot be too small, considering the fabrication accuracy. Therefore, it is difficult to compress the ratio between the stopband and the FSR of the F–P cavity to realize FSR-free response by modifying the mirror strength. Here, to overcome this challenge, we adopt a nanobeam cavity with asymmetric Bragg mirrors, as shown in Figure 1c. The left Bragg mirror (N_L holes with pitch P1) has a different pitch from the right Bragg mirror (N_R holes with pitch P2). Two tapers (with N_{TL} and N_{RL} holes) are utilized to match the mode profiles between the mirror and waveguide adiabatically, minimizing scattering losses at the mirror-cavity interface.

We start by examining the band structures of one unit cell, as plotted in Figure 1d. The blue and red lines correspond to the band structures of the left and right Bragg mirrors, respectively. The corresponding transmission spectra of Bragg mirrors are shown in Figure 1e. For the light in the stopband, a high rejection ratio can be obtained. Otherwise, the light coupled into the cavity will be transmitted to the lower waveguide modes or scattered into the cladding. Evidently, the band structures have an offset due to different Bragg mirror pitches, forming an overlapping band, as illustrated in the green shad region. Therefore, only the light that falls within the effective stopband (overlapping band) can be reflected by both the left and right Bragg mirrors and subsequently amplified in the cavity. By selecting an appropriate overlapping band that is smaller than the FSR of the F–P cavity, it is possible to excite only the fundamental longitudinal mode within the cavity and realize FSR-free response.

To verify the results presented in Figure 1e, we calculated the spectral responses of the Bragg mirror by the 3D finite difference time domain method (3D FDTD). This calculation allows us to determine the lower and upper band edges as functions of the pitch. The blue dashed line indicates the upper edge of the stopband for a pitch of 340 nm, while the red solid curve refers to the lower edges for different pitches, as illustrated in **Figure 2**a. The effective stopband, which is defined as the difference between the blue and red curves, monotonically decreases with increasing pitch. Notably, the upper band edge with a pitch of 340 nm intersects with the lower band edge when the pitch equals 464 nm, resulting in the absence of an overlapping band at larger pitches. Therefore, by modifying the pitch of Bragg mirrors, the overlapping band can be engineered flexibly without significantly increasing the cavity length. We fixed P1 at 340 nm and varied P2 from 340 to 480 nm to calculate the spectral responses of the SCAN cavity, as shown by the black solid curve in Figure 2b. The blue dash and red solid curves represent the transmission spectra of the left and right Bragg mirrors, respectively. When P1 and P2 are both equal to 340 nm, we can observe multiple transmission dips due to multiple longitudinal modes excited in the cavity. As P2 is increased to 400 nm, multiple longitudinal modes continue to coexist within the cavity, although the mode number decreases as the overlapping band narrows. Encouragingly, when P2 is set to 420 nm, only the fundamental longitudinal mode is excited in the overlapping band and only one dip is present within 350 nm from 1300 to 1650 nm. The FSR-free wavelength range can be broader if shorter or longer wavelengths are considered. Further increasing the pitch P2, no dip is observed since there is no overlap between the stopband of the left and right Bragg mirrors.

To achieve FSR-free response, we choose P1 and P2 as 340 and 420 nm, respectively, for further analyses. By grading the size of the central holes, we aim to confine light more efficiently in the smaller volume.[40] The cutoff wavelength defined by the central wavelength of the stopband as a function of the hole position of the nanobeam, is simulated by 3D FDTD, as shown in Figure 2c. The sizes of the left and right holes are 175 × 250 nm^2 and 220 × 250 nm^2, while the central hole is 125 × 75 nm^2. The pitch numbers (N_L, N_{TL}, N_{TR}, and N_R), are 20, 8, 10, and 20, respectively. The detailed dimensions of the SCAN cavity are given in Note S1 (Supporting Information). The width and thickness of the nanobeam are 500 and 220 nm, respectively. The simulated electric field component |E| for the fundamental transverse-electric (TE) mode within the entire structure is illustrated in Figure 2d. For the wavelength of 1400 nm in the stopband of the left Bragg mirror but out of the stopband of the right Bragg mirror, the light coupled into the cavity is reflected by the left Bragg mirror but can propagate through the right Bragg mirror. As a result, the light injected from the input port is transmitted to the C2 port. On the contrary, for the wavelengths of 1600 nm, the light is transmitted to the C1 port since it is in the stopband of the right Bragg mirror but out of the left Bragg mirror. For the wavelengths of 1460 and 1540 nm, which are both in the overlapping band but non-resonant, the light is reflected by the left and right Bragg mirrors. Finally, the light is transmitted to the T1 port. It should be noted that the insertion loss at non-resonant wavelength can be neglected due to the very short coupling length. At the resonant wavelength of 1513.76 nm, the light is efficiently coupled into the cavity and undergoes significant amplification, with little power coupled to the T1 port.

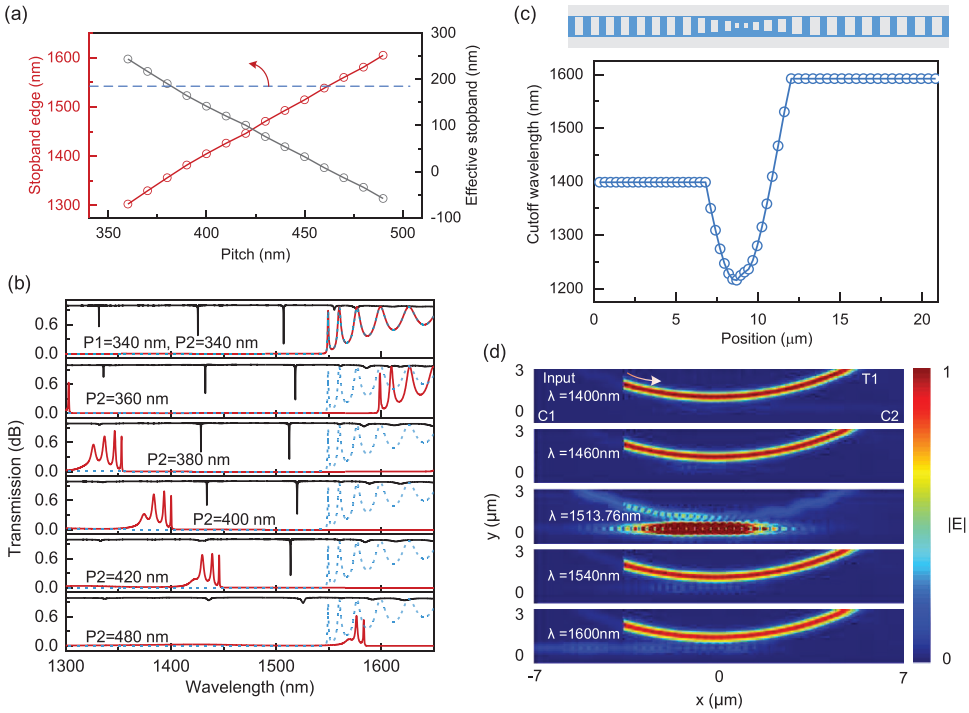

Figure 2. a) Calculated Bragg mirror stopband edges and effective stopbands with different pitches. The blue dashed line shows the upper stopband edge for pitch = 340 nm, while the red solid curve refers to the lower stopband edge for the pitch from 360 to 490 nm. The black solid curve refers to the effective stopband. b) Calculated spectral responses of the SCAN cavity (black solid), and Bragg mirrors (blue dashed, pitch P1 = 340 nm, red solid, pitch = P2) in the wavelength range of 1300–1650 nm. c) Cutoff wavelength as a function of the central hole position of the nanobeam cavity for P1 = 340 nm and P2 = 420 nm. d) Simulated electric field component |E| for the fundamental TE mode in the SCAN cavity (P1 = 340 nm, P2 = 420 nm) at 1400, 1460, 1513.76, 1540, and 1600 nm wavelengths. The arrow indicates the direction of the injected light.

2.2. Device Fabrication and Characterization

The designed devices are patterned on an SOI wafer with a 220-nm top silicon layer by the electron beam lithography (EBL, Raith Voyager, 50 kV) system, fully etched by a single-step inductively coupled plasma (ICP, RIE-101iPH, Samco) dry etching sequentially. A 600-nm-thick silicon dioxide protection layer is deposited by plasma-enhanced chemical vapor deposition on the devices. The scanning electron microscope (SEM, Regulus 8230, HITACHI) images of the fabricated SCAN cavity and grating coupler are exhibited in **Figure 3**a–d. The length of the fabricated SCAN cavity is ≈21 μm. For device characterization, a broadband tunable laser system (Santec full-band TSL, 1260–1630 nm) is utilized to measure the transmission response of the fabricated devices. To increase the detectable bandwidth of the grating coupler, we successively set the fiber tilt coupling angle as $\theta_{\text{fiber}} = 10°$ and 20° to measure the transmission spectra over 1370–1570 nm wavelength ranges. We fabricate a set of SCAN cavities of different parameters. The pitch P1 is set as 340 nm, and P2 is chosen from 340 to 440 nm. The measured spectra are normalized by subtracting the insertion loss of grating couplers, as shown in Figure 3e. For P2 from 340 to 380 nm, multiple dips are excited. For P2 = 400 or 420 nm, we obtain the FSR-free response. We cannot observe an apparent resonant dip when P2 is 440 nm. The measured transmission spectra (blue) and its Lorentz fit curve (red) around the resonant wavelength for P1 = 340 nm and P2 = 400 nm are shown in Figure 3f. The 3-dB bandwidth of the resonant dip is 0.52 nm, while the extinction ratio is 14.5 dB.

The optical microscope images of the SCAN cavity array have a two-dimensional (2D) 5 × 5 layout with only one input and one output port, and all SCAN cavity units share a bus waveguide, as shown in **Figures 4**a,b. The array occupies an area of approximately 215 × 120 μm^2, which can be further reduced by decreasing the spacing of SCAN cavity units. Two 5 × 5 SCAN cavity arrays with varying dip spacings were fabricated for this study. Array A was created with the pitches of the left and right Bragg mirrors ranging from 328 to 352 nm and 388 to 412 nm with 1-nm intervals, while Array B was created with the pitches of the left and right Bragg mirrors ranging from 316 to 364 nm and 376 to 424 nm with 2-nm interval. The coupling gaps of all the cavity units are 220 nm. The normalized transmission spectra of Arrays A and B are illustrated in Figure 4c,d, respectively. The average insertion loss of these two arrays is as low as 3.2 dB across the 1370–1570 nm wavelength range. The insets in these figures provide a close-up view of the resonant wavelengths. There are 25 resonant dips in total for both arrays, which are the largest-channel-count micro-cavity arrays on a single waveguide using waveleghth multiplexing reported to date. Each resonant dip represents a SCAN cavity unit. Figure 4e,f shows the measured resonant wavelength and extinction ratio for each unit in Array A and B. The spectral ranges cover these 25 resonant dips for Array A and B are 55 and 110.5 nm, respectively. The

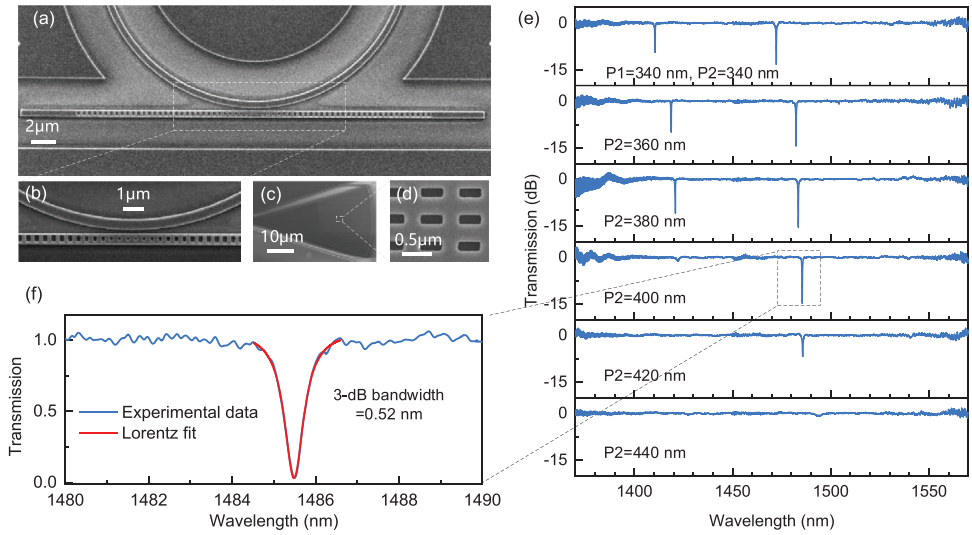

Figure 3. a) SEM image of the fabricated SCAN cavity. b) Zoom-in view of the central coupling region of the SCAN cavity. c,d) SEM image and zoom-in view of the grating coupler. e) Measured transmission spectra of the SCAN cavity for different pitches. f) Measured transmission spectra (blue) and its Lorentz fit curve (red) around the resonant wavelength for P1 = 340 nm and P2 = 400 nm.

variations in extinction ratio among different resonance dips are primarily caused by dispersion. Generally, shorter wavelengths have smaller coupling strengths compared to longer wavelengths for the same coupling gap. Since slight deviations (10 nm) in terms of the hole diameter and waveguide width of the cavity unit are inevitable due to the precision limitations of EBL fabrication, the resonant frequencies of these cavities may not be perfectly aligned. However, post-fabrication trimming or active tuning techniques can be employed to precisely control the position of each resonant dip,[9,47,48] if necessary.

By tracking each dip's wavelength shift, it is possible to determine the local environment at each cavity precisely. Here, a quasi-distributed optical sensing scenario was taken as a proof-of-concept application for the FSR-free SCAN cavity array. In **Figure 5**a, a near-infrared (NIR) light from a tunable laser is used to probe the transmission spectrum of the fabricated SCAN cavity array and the polarization controller controls the polarization state. The output light intensity is received by a power meter connected to a computer, which controls laser scanning and signal processing. The visible laser at 589 nm is irradiated onto

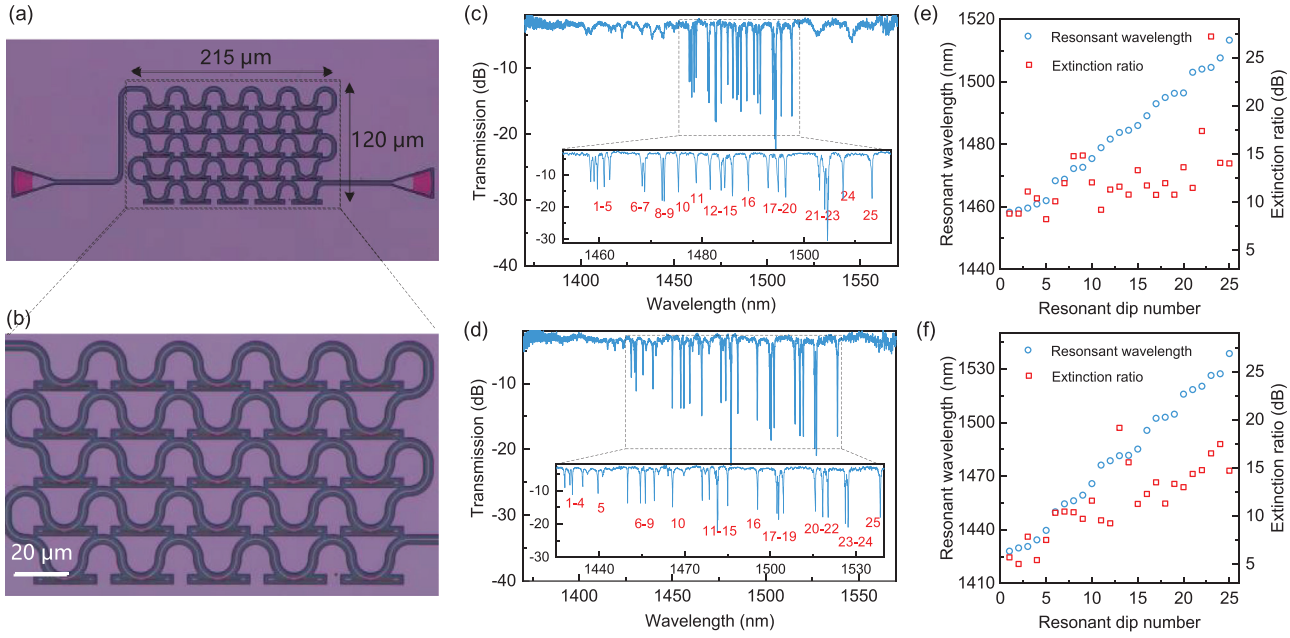

Figure 4. a) Microscope image and b) enlarged image of the 5 × 5 SCAN cavity array. Measured transmission spectra of 5 × 5 SCAN cavity Array A (c) and B (d). The inset shows the 25 resonant wavelengths. Measured resonant wavelength and extinction ratio for each unit in the Array A (e) and B (f).

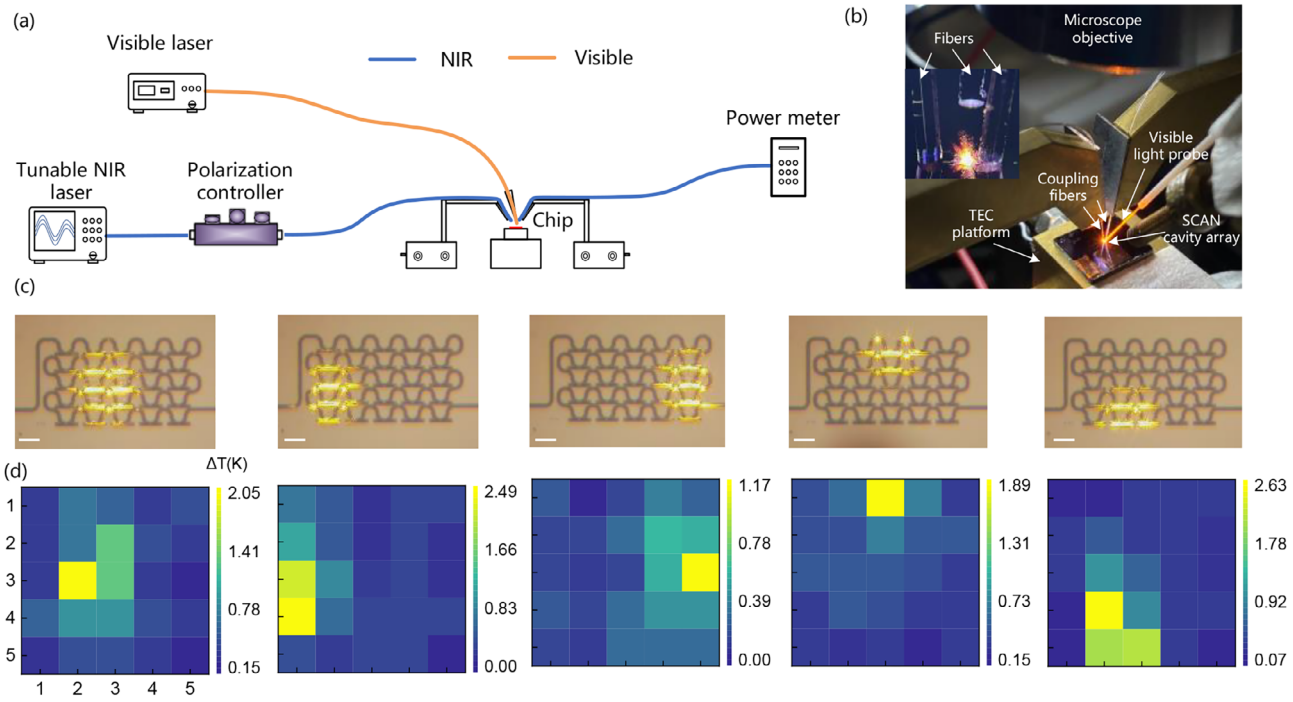

Figure 5. a) Schematic of the setup for quasi-distributed sensing. b) Image of the chip characterization setup. The inset shows the image of coupling fibers and irradiation fiber(middle). c) Images of the visible laser irradiating at different positions of the SCAN cavity array (the first row). Scale bar, 20 μm. d) 2D temperature distribution (the second row). The color bar indicates the temperature change.

the device surface using a traditional single-mode optical fiber (SMF-28) with a 9-μm core diameter. By utilizing an appropriate visible laser power and irradiation distance (150 mW, >100 μm), the photothermal effect of visible light absorption in silicon causes the waveguide temperature to increase, resulting in a redshift of the resonant dips. All performance characterizations were implemented on a thermoelectric cooler (TEC) platform with temperature stability of 0.01 K. A high-magnification microsystem was employed for the irradiation coupling and alignment, as shown in Figure 5b.

Calibration of the resonant dips is required before the quasi-distributed optical sensing demonstration can be performed. To achieve this, we individually irradiate each SCAN cavity and observe the shift in the resonant dips to determine the resonant dip of each SCAN cavity. The experimental results of independent regulation of a single channel are given in Note S2 (Supporting Information). Next, we determine the temperature sensitivity by uniformly heating the chip using the TEC platform and recording the transmission spectra. By linearly fitting each resonance dip shift for different heating temperatures, we can attain the temperature sensitivity of each SCAN cavity. The temperature sensitivity data of each cavity can be found in Note S3 (Supporting Information). To obtain various temperature distributions, we adjust the position of the irradiation fiber and distance from the chip. The first row of Figure 5c showcases the images of the visible laser irradiation at different positions of the SCAN cavity array (center, left, right, up, and down). The images only display relative light intensity distribution to avoid camera overexposure for clarity. By analyzing the wavelength shift of each SCAN cavity and incorporating the temperature sensitivity, we can determine the temperature change of every SCAN cavity. The contour color represents the 2D temperature distribution in Figure 5d, which is consistent with the intensity distribution shown in Figure 5c.

3. Discussion

Table 1 highlights the state-of-the-art on-chip micro-cavity arrays on a single waveguide using wavelength multiplexing. Most of the previously reported WGM cavities had cavity lengths exceeding 100 μm,[2,15] resulting in a maximum FSR of 9 nm. Even when the bending radius was reduced to the limit of 3 μm, the FSR was only 27 nm,[19] and the small bending radius led to significant bending loss, causing larger bandwidths and difficulty in expanding the number of multiplexed cavities on a single waveguide (≤16). In contrast, nanobeam cavities can achieve larger FSRs due to their extremely short cavity lengths.[39,44,45] This allows for a greater number of resonant cavities to be multiplexed along the waveguide. However, the channel count reported in existing nanobeam cavity studies remains limited (≤5). Additionally, the simultaneous excitation of multiple resonant longitudinal modes often restricts the FSR of nanobeam cavities to below 100 nm, thereby limiting the number of cascaded channels. By employing delicate design, the FP cavity can achieve FSR-free responses within a range of 200 nm.[32] However, the structure design involving edge etching results in low grating modulation intensity and large device sizes. Our innovative design fundamentally overcomes the limitations of FSR and achieves FSR-free responses while benefiting from wavelength-scale dimensions of the nanobeam cavity. Remarkably, we have achieved a groundbreaking record of 25 cascaded channels, only covering 55-nm

Table 1. Comparison of reported on-chip micro-cavity arrays on a single waveguide using wavelength multiplexing.

References	Basic units	FSR [nm]	Cavity length [μm]	Channel count	Platforms	Applications
[2]	Micro-ring	5	298	15	SiN	Optical computing
[15]	Micro-ring	8.5	126	15	ChG	Acoustic sensing
[19]	Micro-disk	/	40	4	SOI	Optical computing
[20]	Micro-ring	27	20	16	SOI	Optical communication
[32]	F-P	>200	96	7	SOI	Spectrometer
[39]	Nanobeam	/	8	5	SOI	Biochemical sensing
[44]	Nanobeam	80	8	4	SOI	All-optical switches
[45]	Nanobeam	/	18	3	SOI	Spectrometer
Our work	Nanobeam	>350	21	25	SOI	Temperature sensing

ChG, chalcogenide glass.

spectral range. Considering the extremely low losses of our device and the extensive usable wavelength range (>350 nm), the number of cascaded channels can further increase to hundreds.

4. Conclusion

In conclusion, we have developed a scalable SCAN cavity with asymmetric Bragg mirrors that effectively compresses the overlapping stopband of the left and right Bragg mirrors to overcome the limitation of FSR while maintaining a small footprint. The fabricated SCAN cavity features a single dip in the wavelength range of 1370–1570 nm and a length of only 21 μm, making it easy to scale up to a SCAN cavity array. We have fabricated two 25-SCAN-cavity arrays with varying pitch intervals, all of which are connected by a single bus waveguide. We both observe 25 resonant dips with an average insertion loss of ≈3.2 dB over a broad wavelength range, verifying high-feasibility large-scale integration. Furthermore, we demonstrated the capability of our 25-SCAN-cavity array to enable 2D quasi-distributed temperature sensing by analyzing a single transmission spectrum. The results reveal the opportunities in the studies of high-sensitivity and high-position-resolution optical sensing.

Supporting Information

Supporting Information is available from the Wiley Online Library or from the author.

Acknowledgements

The authors would like to acknowledge Westlake Center for Micro/Nano Fabrication and Instrumentation, Service Center for Physical Sciences (Zhen Yang's assistance in SEM characterization) at Westlake University, and ZJU Micro-Nano Fabrication Center at Zhejiang University for the facility support. The authors would also like to thank Xue Wang for their help in device fabrication. Funding: National Natural Science Foundation of China (62175202, 62205274, 12104375, 61975179, 91950204); Key Project of Westlake Institute for Optoelectronics (2023GD003/110500Y0022303); Zhejiang Provincial Natural Science Foundation of China (LD22F040002); Leading Innovative and Entrepreneur Team Introduction Program of Zhejiang (2020R01005); Special Support Plan for Photoelectric Chips Research at Westlake University (10300000H062201/004); Start-up fund of Westlake University.

Conflict of Interest

The authors declare no conflict of interest.

Data Availability Statement

The data that support the findings of this study are available from the corresponding author upon reasonable request.

Keywords

FSR-free filter, nanobeam cavity, quasi-distributed optical sensing

Received: August 28, 2023
Revised: October 16, 2023
Published online:

[1] R. Ding, Y. Liu, Q. Li, Z. Xuan, Y. Ma, Y. Yang, A. E. J. Lim, G. Q. Lo, K. Bergman, T. Baehr-Jones, M. Hochberg, *IEEE Photonics J* **2014**, *6*, 1.
[2] J. Feldmann, N. Youngblood, C. D. Wright, H. Bhaskaran, W. H. P. Pernice, *Nature* **2019**, *569*, 208.
[3] B. J. Shastri, A. N. Tait, T. Ferreira de Lima, W. H. P. Pernice, H. Bhaskaran, C. D. Wright, P. R. Prucnal, *Nat. Photonics* **2021**, *15*, 102.
[4] C. Li, X. Zhang, J. Li, T. Fang, X. Dong, *PhotoniX* **2021**, *2*, 20.
[5] H. Shu, L. Chang, Y. Tao, B. Shen, W. Xie, M. Jin, A. Netherton, Z. Tao, X. Zhang, R. Chen, B. Bai, J. Qin, S. Yu, X. Wang, J. E. Bowers, *Nature* **2022**, *605*, 457.
[6] M. J. Filipovich, Z. Guo, M. Al-Qadasi, B. A. Marquez, H. D. Morison, V. J. Sorger, P. R. Prucnal, S. Shekhar, B. J. Shastri, *Optica* **2022**, *9*, 1323.
[7] A. A. Jørgensen, D. Kong, M. R. Henriksen, F. Klejs, Z. Ye, Ò. B. Helgason, H. E. Hansen, H. Hu, M. Yankov, S. Forchhammer, P. Andrekson, A. Larsson, M. Karlsson, J. Schröder, Y. Sasaki, K. Aikawa, J. W. Thomsen, T. Morioka, M. Galili, V. Torres-Company, L. K. Oxenløwe, *Nat. Photonics* **2022**, *16*, 798.
[8] B. Corcoran, M. Tan, X. Xu, A. Boes, J. Wu, T. G. Nguyen, S. T. Chu, B. E. Little, R. Morandotti, A. Mitchell, D. J. Moss, *Nat. Commun.* **2020**, *11*, 2568.
[9] A. Jha, C. Huang, T. F. Delima, H.-T. Peng, B. Shastri, P. R. Prucnal, *IEEE J. Sel. Top. Quantum Electron.* **2022**, *28*, 1.
[10] M. Eppenberger, A. Messner, B. I. Bitachon, W. Heni, T. Blatter, P. Habegger, M. Destraz, E. De Leo, N. Meier, N. Del Medico,

C. Hoessbacher, B. Baeuerle, J. Leuthold, *Nat. Photonics* **2023**, *17*, 360.
[11] C. Adamopoulos, P. Zarkos, S. Buchbinder, P. Bhargava, A. Niknejad, M. Anwar, V. Stojanovic, *IEEE Open Journal of the Solid-State Circuits Society* **2021**, *1*, 198.
[12] G. J. Triggs, Y. Wang, C. P. Reardon, M. Fischer, G. J. O. Evans, T. F. Krauss, *Optica* **2017**, *4*, 229.
[13] T.-W. Lu, C.-C. Wu, P.-T. Lee, *ACS Photonics* **2018**, *5*, 2767.
[14] W. J. Westerveld, M. Mahmud-Ul-Hasan, R. Shnaiderman, V. Ntziachristos, X. Rottenberg, S. Severi, V. Rochus, *Nat. Photonics* **2021**, *15*, 341.
[15] J. Pan, Q. Li, Y. Feng, R. Zhong, Z. Fu, S. Yang, W. Sun, B. Zhang, Q. Sui, J. Chen, Y. Shen, Z. Li, *Nat. Commun.* **2023**, *14*, 3250.
[16] L. S. Puumala, S. M. Grist, J. M. Morales, J. R. Bickford, L. Chrostowski, S. Shekhar, K. C. Cheung, *Biosensors* **2023**, *13*, 53.
[17] Sitao Chen, Xin Fu, Jian Wang, Yaocheng Shi, Sailing He, Daoxin Dai, *J Lightwave Technol.* **2015**, *33*, 2279.
[18] A. Van Wijk, C. R. Doerr, Z. Ali, M. Karabiyik, B. I. Akca, *Opt. Express* **2020**, *28*, 14618.
[19] W. Zhang, J. Yao, *Nat. Commun.* **2020**, *11*, 406.
[20] W. Zhao, Y. Peng, X. Cao, S. Zhao, R. Liu, Y. Wei, D. Liu, X. Yi, S. Han, Y. Wan, K. Li, G. Wu, J. Wang, Y. Shi, D. Dai, *Nanophotonics* **2022**, *11*, 4299.
[21] J. Cheng, Y. Zhao, W. Zhang, H. Zhou, D. Huang, Q. Zhu, Y. Guo, B. Xu, J. Dong, X. Zhang, *Front Optoelectron* **2022**, *15*, 15.
[22] F. Morichetti, M. Milanizadeh, M. Petrini, F. Zanetto, G. Ferrari, D. O. De Aguiar, E. Guglielmi, M. Sampietro, A. Melloni, *Nat. Commun.* **2021**, *12*, 4324.
[23] R. Xiao, Y. Shi, J. Li, P. Dai, Y. Zhao, L. Li, J. Lu, X. Chen, *Opt. Express* **2019**, *27*, 1941.
[24] C. Lyu, Z. Liu, Z. Huo, C. Ge, X. Cheng, H.-Y. Tam, *Photonics Res.* **2020**, *8*, 1134.
[25] D. Liu, M. Zhang, D. Dai, *Opt. Lett.* **2019**, *44*, 1304.
[26] N. Eid, R. Boeck, H. Jayatilleka, L. Chrostowski, W. Shi, N. A. F. Jaeger, *Opt. Express* **2016**, *24*, 29009.
[27] D. T. H. Tan, K. Ikeda, Y. Fainman, *Opt. Lett.* **2009**, *34*, 1357.
[28] M. W. Puckett, F. Vallini, A. Grieco, Y. Fainman, *Opt. Lett.* **2015**, *40*, 379.
[29] P. Cheben, J. Ctyroký, J. H. Schmid, S. Wang, J. Lapointe, J. G. Wangüemert-Pérez, I. Molina-Fernández, A. Ortega-Moñux, R. Halir, D. Melati, D. Xu, S. Janz, M. Dado, *Opt. Lett.* **2019**, *44*, 1043.
[30] C. Sun, C. Zhong, M. Wei, H. Ma, Y. Luo, Z. Chen, R. Tang, J. Jian, H. Lin, L. Li, *Photonics Res.* **2021**, *9*, 1013.
[31] C. Sun, Y. Yin, Z. Chen, Y. Ye, Y. Luo, H. Ma, L. Wang, M. Wei, J. Jian, R. Tang, H. Dai, J. Wu, J. Li, D. Zhang, H. Lin, L. Li, *PhotoniX* **2022**, *3*, 12.
[32] C. Sun, Z. Chen, Y. Yin, Y. Ye, Y. Luo, H. Ma, J. Jian, Y. Shi, C. Zhong, D. Zhang, H. Lin, L. Li, *ACS Photonics* **2022**, *9*, 2973.
[33] J. L. O'brien, A. Furusawa, J. Vučković, *Nat. Photonics* **2009**, *3*, 687.
[34] K. C. Balram, M. I. Davanço, J. D. Song, K. Srinivasan, *Nat. Photonics* **2016**, *10*, 346.
[35] K. Fang, M. H. Matheny, X. Luan, O. Painter, *Nat. Photonics* **2016**, *10*, 489.
[36] M. Li, J. Ling, Y. He, U. A. Javid, S. Xue, Q. Lin, *Nat. Commun.* **2020**, *11*, 4123.
[37] Y. Chen, W. S. Fegadolli, W. M. Jones, A. Scherer, M. Li, *ACS Nano* **2014**, *8*, 522.
[38] Q. Qiao, J. Xia, C. Lee, G. Zhou, *Micromachines* **2018**, *9*,
[39] S. Mandal, J. M. Goddard, D. Erickson, *Lab Chip* **2009**, *9*, 2924.
[40] K.-Y. Jeong, Y.-S. No, Y. Hwang, K. S. Kim, M.-K. Seo, H.-G. Park, Y.-H. Lee, *Nat. Commun.* **2013**, *4*, 2822.
[41] Y. Li, J. Zhang, D. Huang, H. Sun, F. Fan, J. Feng, Z. Wang, C. Z. Ning, *Nat. Nanotechnol.* **2017**, *12*, 987.
[42] W. Xie, P. Verheyen, M. Pantouvaki, J. Van Campenhout, D. Van Thourhout, *Laser Photonics Rev.* **2021**, *15*, 2000317.
[43] F. Pyatkov, V. Fütterling, S. Khasminskaya, B. S. Flavel, F. Hennrich, M. M. Kappes, R. Krupke, W. H. P. Pernice, *Nat. Photonics* **2016**, *10*, 420.
[44] G. Dong, W. Deng, J. Hou, L. Chen, X. Zhang, *Opt. Express* **2018**, *26*, 25630.
[45] J. Zhang, Z. Cheng, J. Dong, X. Zhang, *Optica* **2022**, *9*, 517.
[46] D.-Q. Yang, B. Duan, X. Liu, A.-Q. Wang, X.-G. Li, Y.-F. Ji, *Micromachines* **2020**, *11*, 72.
[47] S. Han, Y. Shi, *Opt. Express* **2018**, *26*, 15908.
[48] X. Chen, M. M. Milosevic, D. J. Thomson, A. Z. Khokhar, Y. Franz, A. F. J. Runge, S. Mailis, A. C. Peacock, G. T. Reed, *Photonics Res.* **2017**, *5*, 578.

LASER
& PHOTONICS
REVIEWS

Supporting Information

for *Laser Photonics Rev.*, DOI 10.1002/lpor.202300828

High-Resolution 2D Quasi-Distributed Optical Sensing with On-Chip Multiplexed FSR-Free Nanobeam Cavity Array

Renjie Tang, Chunlei Sun, Kangjian Bao, Zequn Chen, Zezhao Ju, Maoliang Wei, Yingchun Wu, Jianghong Wu, Kai Xu, Hongtao Lin and Lan Li**

Supporting information

High-resolution 2D quasi-distributed optical sensing with on-chip multiplexed FSR-free nanobeam cavity array

Renjie Tang†, Chunlei Sun†, Kangjian Bao, Zequn Chen, Zezhao Ju, Maoliang Wei, Yingchun Wu, Jianghong Wu, Kai Xu, Hongtao Lin, Lan Li**

Supplementary Note 1: Detailed dimensions of the SCAN cavity

The width of the gratings and tapers is set at 500 nm, while the etch thickness is 220 nm. The lengths of left grating, left taper, right grating, and right taper of each channel in Array A and Array B are shown in **Tables S1** and **S2**.

Table S1. Lengths of left grating, left taper, right grating and right taper of each channel in Array A.

Number	Left grating length (μm)	Left taper length (μm)	Right grating length (μm)	Right taper length (μm)
1	6.560	1.879	2.896	7.760
2	6.580	1.886	2.906	7.780
3	6.600	1.894	2.916	7.800
4	6.620	1.901	2.926	7.820
5	6.640	1.909	2.936	7.840
6	6.660	1.916	2.946	7.860
7	6.680	1.924	2.956	7.880
8	6.700	1.931	2.966	7.900
9	6.720	1.939	2.976	7.920
10	6.740	1.946	2.986	7.940
11	6.760	1.954	2.996	7.960
12	6.780	1.961	3.006	7.980
13	6.800	1.969	3.016	8.000
14	6.820	1.976	3.026	8.020
15	6.840	1.984	3.036	8.040
16	6.860	1.991	3.046	8.060

17	6.880	1.999	3.056	8.080
18	6.900	2.006	3.066	8.100
19	6.920	2.014	3.076	8.120
20	6.940	2.021	3.086	8.140
21	6.960	2.029	3.096	8.160
22	6.980	2.036	3.106	8.180
23	7.000	2.044	3.116	8.200
24	7.020	2.051	3.126	8.220
25	7.040	2.059	3.136	8.240

Table S2. Lengths of left grating, left taper, right grating and right taper of each channel in Array B.

Number	Left grating length (μm)	Left taper length (μm)	Right grating length (μm)	Right taper length (μm)
1	6.320	1.789	2.776	7.520
2	6.360	1.804	2.796	7.560
3	6.400	1.819	2.816	7.600
4	6.440	1.834	2.836	7.640
5	6.480	1.849	2.856	7.680
6	6.520	1.864	2.876	7.720
7	6.560	1.879	2.896	7.760
8	6.600	1.894	2.916	7.800
9	6.640	1.909	2.936	7.840
10	6.680	1.924	2.956	7.880
11	6.720	1.939	2.976	7.920
12	6.760	1.954	2.996	7.960
13	6.800	1.969	3.016	8.000
14	6.840	1.984	3.036	8.040
15	6.880	1.999	3.056	8.080
16	6.920	2.014	3.076	8.120
17	6.960	2.029	3.096	8.160

18	7.000	2.044	3.116	8.200
19	7.040	2.059	3.136	8.240
20	7.080	2.074	3.156	8.280
21	7.120	2.089	3.176	8.320
22	7.160	2.104	3.196	8.360
23	7.200	2.119	3.216	8.400
24	7.240	2.134	3.236	8.440
25	7.280	2.149	3.256	8.480

Supplementary Note 2: Experimental results of independent regulation of a single channel

Calibration of the resonant dips is required before the quasi-distributed optical sensing demonstration can be performed. To investigate this, the visible light laser was directed towards a specific position of a single nanobeam cavity, and the response of each nanobeam cavity to the laser was measured individually. The experimental results, which demonstrate the independent regulation of a single channel, are presented in **Figure S1**. When a single resonant cavity was focused on with a spot diameter of approximately 10 μm, a significant red shift in the corresponding resonant dip was observed, while all other dips remained nearly unchanged. This phenomenon is illustrated in **Figure S1**, indicating minimal interference between the channels of the cascaded device. This can be attributed to the nanobeam cavity confining the optical field within a very small region. Although our device may appear compact, it is insufficient to cause optical crosstalk between different channels. Furthermore, we estimated the modal volume of the cavities by inserting the calculated electric field distributions into the following equation[1]:

$$V = \frac{\int \varepsilon(\boldsymbol{r})|E(\boldsymbol{r})|^2 d^3\boldsymbol{r}}{\max[\varepsilon(\boldsymbol{r})|E(\boldsymbol{r})|^2]}, \quad (1)$$

where $\varepsilon(\boldsymbol{r})$ is the dielectric constant and $E(\boldsymbol{r})$ is the electric field. The integration region in **Equation (1)** covers the entire length of the nanobeam cavity in the x-direction, spans 1.5 μm in the y-direction, and extends 1 μm in the z-direction from the center of the cavity. The calculated mode volume is ~0.101 μm^3, while the distance between the centers of the two adjacent cavities is larger than 25 μm.

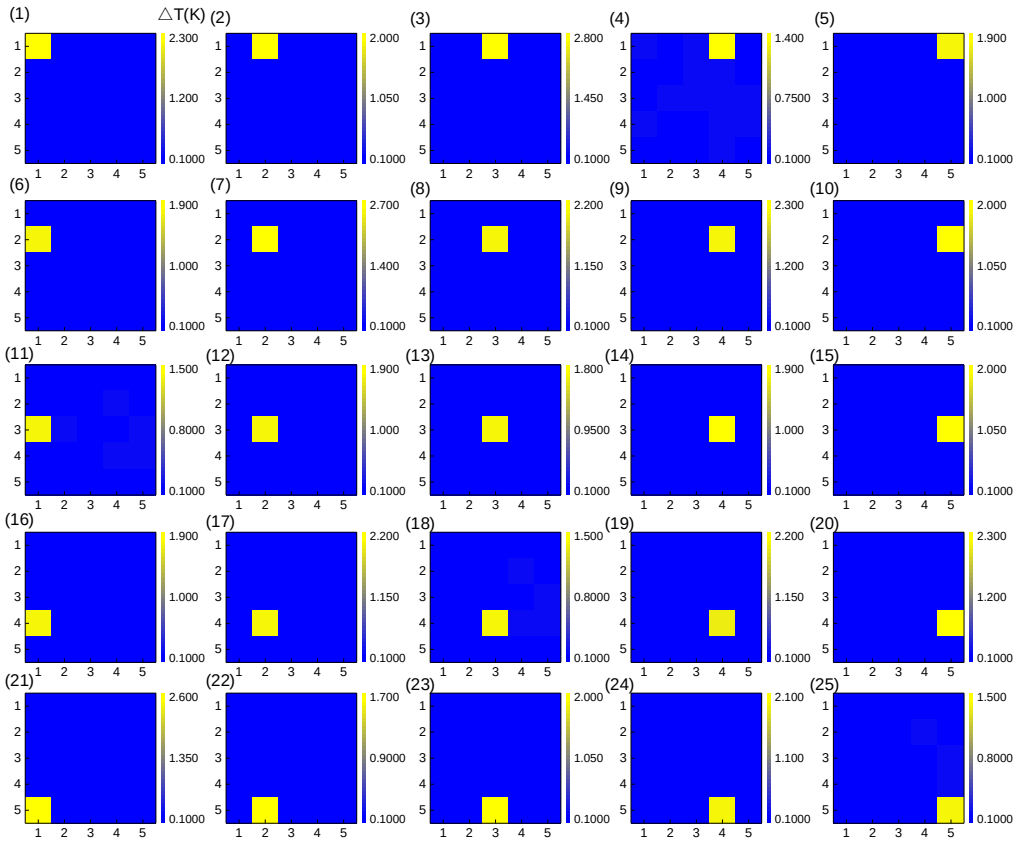

Figure S1. 2D temperature distribution from the irradiation of the visible laser at each individual nanobeam cavity. The color bar represents the corresponding temperature change.

Supplementary Note 3: Temperature sensitivity of each cavity

The chip was uniformly heated using the thermoelectric cooler (TEC) platform, and the transmission spectra were recorded. The resonant wavelengths were extracted, and linear fitting analysis was performed to obtain the temperature sensitivity of each cavity. The temperature sensitivity data are presented in **Figure S2**.

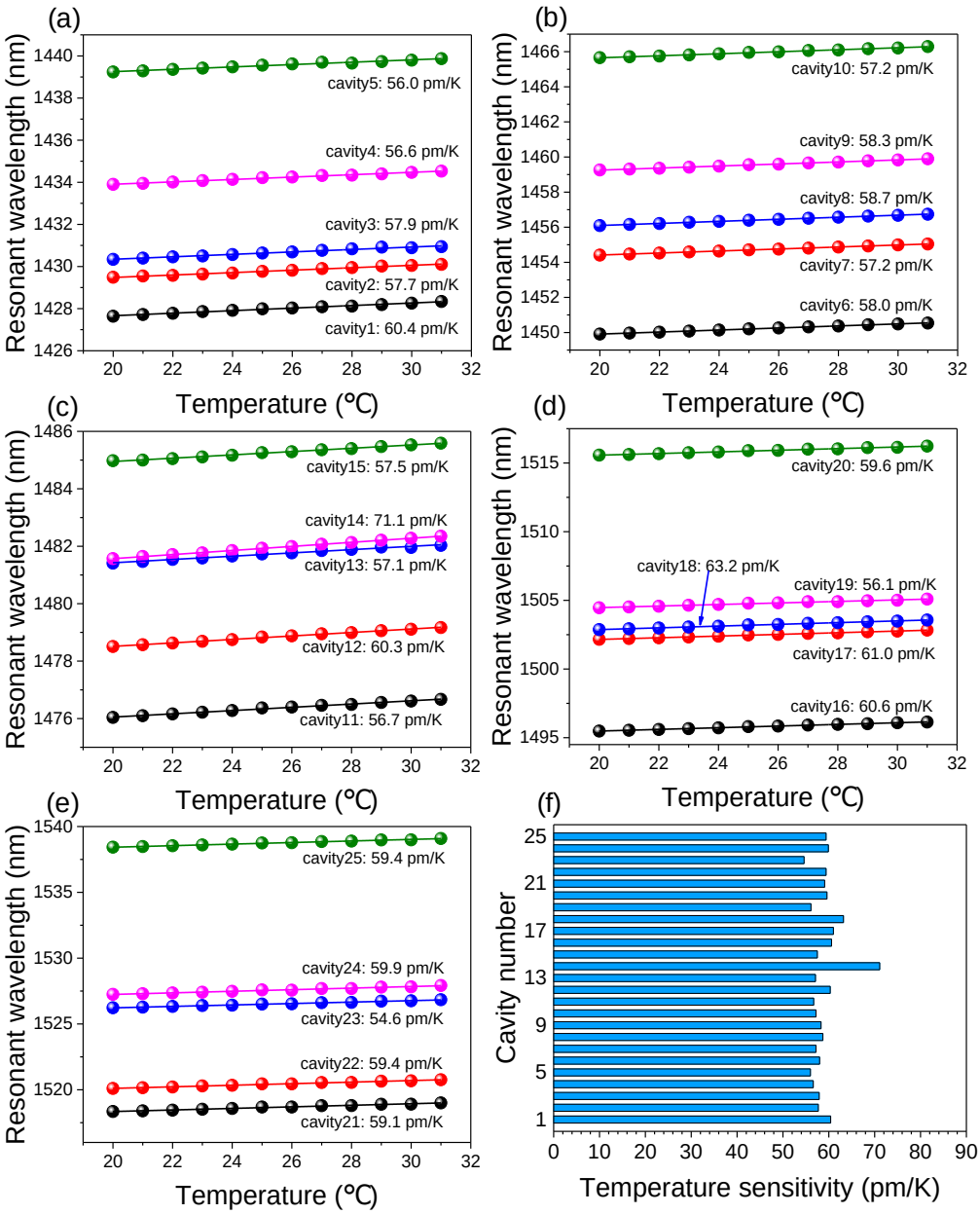

Figure S2. Temperature sensitivity of each cavity. (a) Cavities 1-5; (b) Cavities 6-10; (c) Cavities 11-15; (d) Cavities 16-20; (e) Cavities 21-25; (f) Histogram summary of the temperature sensitivity for each cavity.